CrystEngComm

Accepted Manuscript

ROYAL SOCIETY OF CHEMISTRY

www.rsc.org/crystengcomm

$(Co_xMg_{1-x})O$ nanocondensates by pulsed laser ablation of bulk alloy in air

Bang-Ying Chen,[a] Shih-Siang Lin,[a] Pouyan Shen[a] and Shuei-Yuan Chen*[b]

[a]*Department of Materials and Optoelectronic Science,*

National Sun Yat-sen University

Kaohsiung, 80424 Taiwan, R.O.C.

[b]*Department of Mechanical and Automation Engineering*

I-Shou University

Kaohsiung, 84001 Taiwan, R.O.C.

* *To whom correspondence should be addressed, e-mail: steven@isu.edu.tw*

Abstract

Pulsed laser ablation of bulk CoO-MgO (solid solution in 1:9, 1:1, 9:1 molar ratio) in air was used to fabricate alloyed nanocondensates for X-ray diffraction, transmission electron microscopy and UV-visible absorption characterizations. The nanocondensates were formed as rocksalt-type $(Co_xMg_{1-x})O$ protoxide with well-developed {100} faces for coalescence as single crystal or (100) twist boundary with misorientation by 26.6°. Additional Mg-doped (8 at.%) $Co_{3-\delta}O_4$ spinel in the form of cubic nanocondensates and nearly spherical particulate with {011} and {121} facets were produced from Co-rich target. The predominant $(Co_xMg_{1-x})O$ protoxide nanocondensates were able to turn the carbonaceous support into turbostratic graphene shell upon radiant heating and showed tailored paracrystalline distribution of defect clusters (ca. 1.5-2 nm interspacing), internal compressive stress (up to ca. 2 GPa), and UV absorption (3.2-3.5 eV) for potential opto-electronic catalytic applications.

1. Introduction

This research is about the dynamic condensation of $(Co_xMg_{1-x})O$ protoxide and Mg-doped $Co_{3-\delta}O_4$

spinel via a dynamic pulsed laser ablation (PLA) route in air regarding their defect nanostructures, shape, special interface, internal stress and optical properties.

$Co_{1-x}O$ with a considerable extent of nonstoichiometry (x ~0.01)[1] was known to form $Co_{3-\delta}O_4$ spinel by cooling below 900°C in air.[2] The $Co_{3-\delta}O_4$ changes from the normal spinel structure at low pressures to a partially inverse spinel structure at pressures above 17.7 GPa presumably involving the interaction of charges between tetrahedral and octahedral sites via a charge transfer process.[3] The MgO-$Co_{1-x}O$ binary forms a complete solid solution at high temperatures in air and decomposes below 850°C into Mg-doped (<1 at %) $Co_{3-\delta}O_4$ spinel and protoxide of a wide Co/(Mg+Co) atomic ratio decreasing drastically from 99% to ca. 2% upon cooling from 850°C to 600°C in air according to the phase diagram (ref.[4] cf. also Fig. 51 of ref.[5]). Nevertheless, $Co_{3-\delta}O_4$ spinel with a considerably higher Mg^{2+} content up to ca. $MgCo_2O_4$ composition for $P(O_2)$ = 0.21 atm was documented in FACT oxide database (Appendix 1) and stoichiometric $MgCo_2O_4$ with an almost ideal inverse spinel structure was metastabilized by coprecipitation in aqueous solution.[6] Besides, paracrystal was known to reside in the protoxide and spinel structure at temperatures for Co-rich composition. In fact, both $Co_{1-x}O$ and $Co_{3-\delta}O_4$ spinel form paracrystal when doped with Zr^{4+},[7] although undoped $Co_{3-\delta}O_4$ spinel was found surprisingly to have paracrystalline distribution of defect clusters.[8] The Mg-doped $Co_{3-\delta}O_4$ spinel was also found to possess paracrystalline distribution of defect clusters for bulk sample prepared by sintering and then annealing.[9, 10] On the other hand, the bulk MgO dissolved with $Co_{1-x}O$ has a rather complicated planar diffraction contrast,[9] which is different from the G.P. zone observed in bulk Ti-doped MgO.[11]

Nanoparticles of cobalt oxides in rock salt- or spinel-type structure of various shape were commonly fabricated by coprecipitation,[12] a sol-gel route,[13] liquid-liquid interface or microemulsion involving surfactant[14] and hydrothermal/solvothermal method.[15,16] Recently the synthetic strategies and characteristics of morphology-controlled Co_3O_4 nanomaterials from cobalt hydroxide precursors

with zero- to two-dimensional and hierarchical nanostructures were reported.[17] The synthesis of unusual single-crystal Co_3O_4 nanocages with highly exposed {110} reactive facets was further accomplished via a one-step solution method.[18] Such nanocages were shown to deliver a high reversible lithium storage capacity and exhibit an excellent rate capability due to the dominantly exposed {110} planes, a high density of atomic steps in nanocages, and the large void interiors.[18] In this connection, Co_3O_4 nano octahedrons with {111} planes also show better cyclic and rate properties than nanocubes with {001} planes.[19] It was also reported that a high capacity of 380 mAg^{-1} at a high current density of 1000 mAg^{-1} can be delivered by a Co_3O_4 nanomesh with exposed {112} high energy facets.[20] The MgO-CoO binary is an effective catalyst when prepared in the form of nanoparticles with predominant rocksalt- and minor spinel-type structure by the aerogel method.[21] It is thus of interest to fabricate $(Co_xMg_{1-x})O$ nanocondensates and particulates by the dynamic PLA process to have specific phase assemblage and particle size for potential catalytic applications of other investigators. (The dynamic PLA process was recently used for the syntheses of optocatalytically and electronically important materials such as Au nanospheres through a laser irradiation-induced shape coversion,[22] tungsten oxide (WO_3) nanostructures by laser ablation of W in water and a subsequent hydrothermal route,[23] epitaxial AlN (0001) film on Al(111) substrate[24] and GaN film via an AlN buffer layer on Cu(111) substrate.[25])

As for an alternative clean/dynamic synthesis, PLA of Co target in an oxygen background gas has been used to condense $Co_{1-x}O$ nanocrystals with cubic shape yet negligible defect clusters and hydroxylation.[26] Such $Co_{1-x}O$ nanocrystals tended to coalesce over the cube {100} faces to form nano-chain aggregate or in a closer packed manner.[26] It is not clear if Mg^{2+} spiking affects significantly the paracrystal and/or G.P. zone formation in $Co_{1-x}O$ protoxide and $Co_{3-\delta}O_4$ spinel when fabricated as nanocondensates by a PLA route. It is also of interest to characterize the shape of the nanocondensates and hence their (hkl)-specific coalescence to form special grain boundary.

Here, the PLA method was adopted to fabricate alloyed nanocondensates of $(Co_xMg_{1-x})O$ protoxide and Mg-doped $Co_{3-\delta}O_4$ spinel focusing on the tailored shape, defect nanostructures (in particular paracrystal and special interface), internal stress and UV-visible absorption properties as of concern to their potential optocatalytic applications in air by other investigators and their possible occurrence in natural dynamic settings.

2. Experimental

The $(Co_{0.1}Mg_{0.9})O$, $(Co_{0.5}Mg_{0.5})O$ and $(Co_{0.9}Mg_{0.1})O$ solid solution targets (hereafter refer to C1M9, C5M5 and C9M1 for the specified molar ratios) were prepared as well-sintered disks (16 mm x 3 mm in size) by firing the dry-pressed (650 MPa) end member powders (ca. 1 g) in an open air furnace at 1600^{o}C for 5 h and then cooling in the furnace. The reactively sintered disks with rocksalt-type $(Co_xMg_{1-x})O$ solid solution except C9M1 having additional Mg-doped $Co_{3-\delta}O_4$ spinel (cf. Supplement Fig. 1) were subjected to energetic Nd-YAG-laser (Lotis, 1064 nm, beam mode: TEM00) pulse irradiation in air. In such PLA experiments, laser beam was focused to a spot size of 0.03 mm^2 on the sintered disks under 1064 nm excitation at pulse energy of 1100 mJ/pulse. The free run mode for specified pulse duration of 240 μs was adopted to achieve a peak power density of $1.5x10^7$ W/cm^2 at 10 Hz. (We follow the European standard E207/E208 for the selection of laser goggle to protect the naked eyes during laser beam alignment and subsequent PLA experiments which were conducted in an open air chamber coupled with venting system, allowing laser beam incidence through a window yet effectively blocking the scattered laser plumes, heat, light and smoke, if any.) We focused on the effect of target composition, rather than laser parameters, on the morphology, stoichiometry and crystal structure of the nanocondensates and particulates.

The condensates/particulates produced by the above PLA method were deposited on silica glass plate for X-ray diffraction (XRD, SIEMENS D5000, Cu Kα at 40 kV, 30 mA and 3 s for each 0.05^o increment from 15 up to 80 degrees of 2θ angle) and optical polarized microscopic

observations. The crystal structures of the individual condensates collected on Cu grids overlaid with a carbon-coated collodion film were characterized by transmission electron microscopy (TEM, JEOL 3010 at 200 kV) based on bight field image (BFI) and selected area electron diffraction (SAED) and lattice image coupled with 2-D Fourier transform. We avoided using a preheated crystalline substrate for the present PLA study. The reason for using alternative deposition strategies is to have enough deposit on an inert glass substrate for XRD and well-dispersed particles on an amorphous carbonaceous film for TEM characterization. The internal compressive stress of the nanocondensates was estimated from the refined electron diffraction lattice parameters using the Birch-Murnaghan equation of state[27, 28] and the interpolated compressibility data of the end members MgO[29, 30] and CoO.[31]

The UV-visible absorption of the particulates/condensates as-formed by the above PLA process for deposition on silica glass plate was characterized by the instrument of U-3900H, Hitachi, with a resolution of 0.1 nm in the range of 190 to 900 nm.

3. Results

Under naked eye, the solid solution targets C1M9, C5M5 and C9M1 are pink, dark and gray in color, respectively, whereas the laser ablated trough is darkish (Appendix 2). SEM SEI further showed the intact solid-state sintered grains are ca. 10 to 20 μm in size with inter- and intragranular pores in the intact area, which is in drastic contrast to the finer recrystallized grains with decorated whiskers and the solidified molten droplets/flow near the crater by the PLA (cf. Supplement Fig. 2 for the representative C5M5 specimen). This indicates that rapid condensation and solidification of the laser plume ejected from the crater at ca. 2400^{o}C (cf. the liquidus of the C5M5 composition in Appendix 1) has occurred to account for the formation of nanocondensates and particulates as identified in the following.

3.1. XRD

The PLA samples deposited on silica glass plate were identified by XRD to be rocksalt-type $(Co_xMg_{1-x})O$, except C9M1 specimen which has minor Mg-doped $Co_{3-\delta}O_4$ spinel in (Fig. 1). The (200)/(111) count ratio of the $(Co_xMg_{1-x})O$ protoxide is considerably lower for C9M1 than other specimens which may be attributed to shape and phase change of the deposited particles as characterized by TEM.

3.2. TEM

3.2.1. C1M9

Rocksalt-type $(Co_xMg_{1-x})O$ condensates/particulates with cubic shape and hence [100] preferred orientation were assembled by PLA of C1M9 in air for 5 sec as indicated by TEM BFI, DFI and SAED pattern in Fig. 2a, 2b and 2c, respectively. There is bimodal size distribution of the particles, the larger ones (20-60 nm) being rapidly solidified particulates whereas the smaller ones (<15 nm) condensed from atom clusters in the plume of the C1M9 specimen. Such a size distribution is also pertinent to the C5M5 and C9M1 specimen (cf. Supplement Fig. 3). The individual $(Co_xMg_{1-x})O$ particulate with atomic ratio Co:Mg=1:19 deviating from the original target composition due to varied plume composition is cubic-like having {110} ledges still decorated with {100} facets (Fig. 3). In this case, there are several cubic nanocondensates in parallel epitaxy with the particulate despite the surrounding of turbostratic graphene. As addressed later, this can be explained by a {100}-specific coalescence event of the nanoparticles and the catalytic effect of such nanoparticles on the supporting carbon-coated collodion film to form graphene upon radiant heating of the PLA process. Lattice image coupled with 2-D forward/inverse Fourier transform (Fig. 4) further showed parallel epitaxy coalescence of the cubic $(Co_xMg_{1-x})O$ nanocondensates in the [100] zone axis despite the turbostratic graphene shell which was vulnerable to electron dosage. The paracrystalline distribution of defect clusters in this case was manifested by the dark/bright dot-like contrast with 1.5-2 nm interspacing on the average (Fig. 4d).

3.2.2. C5M5

Figs. 5a to 5d compile, respectively the TEM BFI, DFI, SAED pattern and EDX spectrum of a rocksalt type $(Co_xMg_{1-x})O$ particulate with Co:Mg~1.4:1.0 as formed by PLA of C5M5 in air for 5 sec. This particulate has several smaller-sized nanocondensates in coalescence over its (100) top view face to show varied Bragg diffraction contrast. A special grain boundary, i.e. (100) 26.6^o twist boundary, was manifested by lattice image (Fig. 5e) and 2-D Fourier transform of such a nanoparticle slightly off the [100] zone axis (Fig. 5f). Such an unusual twist boundary is apparently a local energy minimum of the interface for the nanocondensates coalesced by the (100) surface during the PLA process. Another $(Co_xMg_{1-x})O$ particulate with different composition (Co:Mg~10:1) were in coalescence with other isostructured particles to exhibit (100), (111) and~$(3\bar{1}\bar{1})$ faces as shown edge on in the $[01\bar{1}]$ zone axis despite turbostratic graphene surrounding when subjected to PLA for 15 sec (Fig. 6). A nearly spherical rocksalt-type $(Co_xMg_{1-x})O$ particulate with Co:Mg~0.9:1.0 on the average and (100) and (011) facets were also found in this specimen to follow parallel epitaxy with a faceted nanocondensate by the oriented attachment over (100) face (Fig. 7). This particulate has paracrystalline distribution of defect clusters with 1.5-2 nm interspacing on the average as manifested by the side band diffractions (Fig. 7c).

3.2.3. C9M1

Fig. 8a to 8c are respectively the TEM BFI, SAED pattern and EDX spectrum of two rocksalt-type $(Co_xMg_{1-x})O$ nanocondensates with a homogenized composition Co:Mg~8.3:1.0, which were coalesced over (100) to have a 2:1 aspect ratio in the [100] zone axis despite again the turbostratic graphene surrounding when formed by PLA of C9M1 in air for 5 sec. The paracrystalline distribution of defect clusters were much better developed in this sample to cause orthogonal planar diffraction contrast with 1.5-2 nm interspacing in the BFI (Fig. 8b).

This Co-rich specimen showed additional Mg-doped $Co_{3-\delta}O_4$ spinel, which typically occurred as cubic-like nanocondensate with Co:Mg~11.3:1.0 having side-band paracrystal diffraction in the [100] zone axis (Fig. 9) or as spherical-like particulate with Co:Mg~11:1, {011}/{121} facets and paracrystal diffraction as shown in the $[11\bar{1}]$ zone axis in Fig. 10. The paracrystalline defect clusters account for the extra diffraction spots which correspond to 1.5-2 nm interspacing in accordance with that observed in Fig. 4d.

3.3. UV-visible absorption and optical polarized microscopy

The UV-visible absorption spectra of the samples produced by PLA of C1M9, C5M5 and C9M1 for 5 min in air show absorbance peaks with extrapolation to 350, 375 and 390 nm corresponding to an apparent minimum band gap of 3.5, 3.3 and 3.2 eV, respectively (Figs. 11a, b and c) under the influence of charge transfer via the Co-based oligomers or complex in MgO-rich specimens. The additional absorbance in Fig. 11a was presumably a result of composition inhomogeneity of the $(Co_xMg_{1-x})O$ particulates/condensates although it is difficult if not impossible to correlate the optical data to specific structures.

Optical polarized microscopic observations indicated the predominant rocksalt-type $(Co_xMg_{1-x})O$ condensates/particulates assembled on a silica glass plate by PLA of C1M9, C5M5 and C9M1 in air for 5 min are brownish with slight birefringence (Fig. 12).

4. Discussion

4.1. Defect chemistry and paracrystalline distribution of defect clusters

Paracrystalline distribution of defect clusters was found to occur in the nanocondensates and particulates of $(Co_xMg_{1-x})O$ protoxide. Such defect clusters can be rationalized by the defect chemistry in the rocksalt-type structure with specific point defect species as in the following.

A smaller lattice parameter for MgO (0.4211 nm, JCPDS file 45-0946) than CoO (0.4261 nm, JCPDS file 75-1550) indicated that Mg^{2+} (effective ionic radii, 0.0720 nm) was replaced by Co^{2+} in high spin (0.0745 nm) rather than low spin state (0.066 nm) in CN 6[32] of the rocksalt-type structure. The oversized dopant Co^{2+} in the Mg^{2+} site could also force further Co ion to enter the interstitial site as $Co_i^{\bullet\bullet\bullet}$, which then induced charge-compensating cation vacancies and 4:1 defect clusters through the following equation in Kröger-Vink notation:[33]

$$CoO \xrightarrow{MgO} Co_{Mg}^{X} + [Co_i^{\bullet\bullet\bullet} + 4\,V_{Co}'' + 5h^{\bullet}] + O_O^{x} \qquad (1)$$

Here Co_{Mg}^{x} signifies a noncharged cobalt at magnesium sites in the crystal lattice and h could be associated with V_{Co}'' to form V_{Co}' or associated with Co_{Mg}^{x} to form $Co_{Mg}^{\bullet}$. The resultant 4:1 type defect clusters can then be assembled to form paracrystalline ordered state in $(Co_xMg_{1-x})O$ protoxide and then occasional Mg-doped $Co_{3-\delta}O_4$ spinel with a specified interspacing (1.5 to 2 nm on the average) of defect clusters in the individual nanoparticles. Alternatively, MgO may be directly doped with Co^{3+} by the following equation:

$$Co_2O_3 \xrightarrow{MgO} Co_{Mg}^{\bullet} + [Co_i^{\bullet\bullet\bullet} + 4\,V_{Co}'' + 4h^{\bullet}] + O_O^{x} \qquad (2)$$

As for the paracrystal hosted by the nanocondensates and particulates of Mg-doped $Co_{3-\delta}O_4$ spinel, its formation would involve Co^{3+} residence in the interstitial tetrahedral site below 900°C to form 4:1 clusters and hence paracrystal in the spinel-type structure of $Co_{3-\delta}O_4$ even without Mg^{2+} dopant.[8] The uptake of Mg^{2+} dopant has significantly raised the defect cluster concentration and hence shortened their interspacing down to ca. 1.5 nm for the present $Co_{3-\delta}O_4$ spinel particulates and nanocondensates in comparison with 2 nm for bulk sample with Co:Mg=8:2 as prepared by a reactive sintering coupled with sublimation route.[10] Such defect cluster enhancement may have something to do with the nanosize effect and internal compressive stress as a result of rapid

heating-cooling of the PLA process.

4.2. Internal stress of the rocksalt-type nanocondensates

The refined XRD lattice parameter of the predominant $(Co_xMg_{1-x})O$ protoxide in C1M9, C5M5 and C9M1 samples are 0.4217 nm, 0.4243nm and 0.4259 nm, respectively before PLA, whereas 0.4209 nm, 0.4224 nm and 0.4241 nm, respectively after PLA under a power density of $1.5x10^7$ W/cm^2 for 5 min in air. The lattice parameter changes in the target post test can be attributed to internal stress rather than negligible change of stoichiometry. The internal compressive stress of the $(Co_xMg_{1-x})O$ protoxide by such a PLA process was then estimated from the refined X-ray lattice parameters to be ca. 0.93, 2.35 and 2.32 GPa, respectively using the Birch-Murnaghan equation of state[27, 28] and the interpolated compressibility data of the end members MgO (B_o=160 GPa and B_o'=4.15)[29] and CoO (B_o=180 GPa and B_o'=3.82).[31] It is not clear if a relatively low internal compressive stress for the $(Co_xMg_{1-x})O$ nanocondensates and particulates in C1M9 specimen has anything to do with their hydroxylation relaxation of the magnesia component in open air condition.

4.3. Shape and special grain boundary of $(Co_xMg_{1-x})O$ nanocondensates

The rocksalt-type $(Co_xMg_{1-x})O$ nanocondensates as produced by PLA of C1M9, C5M5 and C9M1 target in air showed the surface preference {100}> {110}> {111}~ {021}~ {013}~ {311}. The undoped MgO also has the preference {100}> {110}> {111} in unhydroxylated state although {111}, {310} and {110} are more stable than {100} under hydroxylated condition.[30] This indicates that the present rocksalt-type CoO-MgO alloy nanocondensates have negligible composition dependent surface selection and were hardly hydroxylated by the PLA process in air. As for the Mg-doped $Co_{3-\delta}O_4$ nanocondensate in C9M1 based sample, it also favored cubic shape although {011}, {111} and {121} facets were noted when in coalescence with other nanocondensates with rocksalt- and/or spinel-type structures (Fig. 10).

Regarding the {100}-based special grain boundary of the present rocksalt-type $(Co_xMg_{1-x})O$ nanocondensates, it is of interest to note that a sublimation-condensation process at 1500°C also caused cube-like CoO crystallites to deposit preferentially on the (100) surface of the reaction sintered CoO-MgO grains following parallel or 45°-off crystallographic relationship via Brownian motion of the crystallites.[10] The coincidence site lattice (CSL) of such low-energy (100)-specific twist boundary were further documented for the case of $Ni_{1-x}O$ particles within CaO grains[31] and CoO crystallites on CoO-MgO solid solution grains.[10]

Here, a new (100) twist boundary off by 26.6° from stable parallel epitaxy were observed in the rocksalt-type $(Co_xMg_{1-x})O$ nanocondensates as produced by PLA of C9M1 in air. As shown by a schematic drawing in Fig. 13, the (100) 26.6° twist boundary has a rhombohedral CSL with 4.5x lattice parameter of the parental rocksalt-type structure as defined by alternating mixed/unmixed charge along both $2[2\bar{1}0]_A//4.5[100]_B$ and $4.5[010]_A//2[120]_B$ directions.

The interatomic Coulombic interactions is also of concern to the formation of cation-anion mixed (100) surfaces for MeO-MgO alloy in rocksalt-type structure where Me is a specific divalent transition metal ion. The size-mismatched Mg and Co ions are expected to affect the interatomic Coulombic interactions of the cation-anion mixed surface as the driving force for oriented attachment to form special grain boundaries, such as the present {100} twist boundary. It is an open question if solute trapping/segregation occurred at such interface to cause space charge and special paracrystalline distribution of defect clusters different from that of the crystal interior.

4.4. Implication

The rocksalt- and spinel-type nanocondensates with alloyed composition, tailored paracrystalline distribution of defect clusters ca.1.5-2 nm interspacing, and internal compressive stress up to ca. 2 GPa as fabricated by the present PLA route shed light on defect cluster and dynamic phase behavior

of the $Co_{1-x}O$-MgO system in air and even in the interior of the Earth where cobalt may possibly replace iron in the predominant magnesiowüstite in view of the Fe-Co-Ni content in some planetary materials.[36]

As for engineering/industrial implications, the composite oxide nanocondensates in the $Co_{1-x}O$-MgO system may have many potential optocatalytic applications taking advantage of the tailored shape and defects different from the undoped cobalt oxides in thin film or bulk,[37-40] although unfortunately the yields of the particulates/nanocondensates by the present PLA process were too little (mg scale) to study their specific optocatalytic reactions. (Bulk cobalt oxides in rock salt- or spinel-type structure have been used as gas sensors,[41, 42] high-temperature solar selective absorbers[38] and electrochromic devices.[39]) In any case, the densified Mg-doped $Co_{1-x}O$ and/or $Co_{3-\delta}O_4$ spinel with tailored paracrystalline distribution of defect clusters and special interface with space charge are expected to affect charge transfer and hence catalytic activity for step-wise sensor of oxygen partial pressure at high temperatures and other potential opto-electronic catalytic applications such as graphene synthesis. This is supported by the prevailed graphene shell around the as-formed $(Co_xMg_{1-x})O$ nanocondensates when subjected to little electron dosage (Fig. 4a) but not the $(Mg_{0.9}Fe_{0.1})O$ nanocondensates as prepared by the same PLA method and observed under the same TEM condition.[41] In this connection, it is of interest to note that nanocrystalline Co/MgO and has been used to catalyze the formation of carbon nanotubes from various hydrocarbons.[42-44] The $(Co_xMg_{1-x})O$ protoxide nanocondensates especially the C1M9 and C5M5 specimens were also found to catalyze the carbonaceous support to form turbostratic graphene shell upon radiant heating in the present PLA process. Still, further study is required to produce adequate amount of the composite oxide nanocondensates in the $Co_{1-x}O$-MgO system in order to verify their optocatalytic performance.

5. Conclusions

1. PLA of CoO-MgO solid solutions in air caused the formation of dense rocksalt-type

$(Co_xMg_{1-x})O$ protoxide and additional Mg-doped (8 at.%) $Co_{3-\delta}O_4$ spinel from Co-rich target.

2. The $(Co_xMg_{1-x})O$ protoxide has tailored paracrystalline distribution of defect clusters (ca.1.5-2 nm interspacing), internal compressive stress (up to ca. 2 GPa) and well-developed {100} faces for coalescence as (100) 26.6° twist boundary with a fair coincidence site lattice.
3. The $(Co_xMg_{1-x})O$ protoxide nanocondensates were able to catalyze the carbonaceous support to form turbostratic graphene shell upon radiant heating in the PLA process.
4. The paracrystalline Mg-doped (8 at.%) $Co_{3-\delta}O_4$ spinel occurred as cubic nanocondensates and nearly spherical particulate with {011} and {121} facets.
5. The overall nanocondensates and particulates have an apparent minimum band gap decreasing down to ca. 3.2 eV with increasing Co content for potential opto-electronic catalytic applications.

Acknowledgments: This research was supported by Center for Nanoscience and Nanotechnology at NSYSU and partly by the Ministry of Science and Technology, ROC. We thank anonymous referees for constructive comments.

References

1 S.M. Tomlinson, C.R.A. Catlow and J.H. Harding, *J. Phys. Chem. Solids*, 1990, 51, 477.

2 M. Oku and Y. Sato, *Appl. Surf. Sci*., 1992, 55, 37.

3 L. Bai, M. Pravica, Y. Zhao, C. Park, Y. Meng, S.V. Sinogeikin and G. Shen, *Journal of Physics: Condensed Matter*, 2012, 24, 435.

4 J. Robin, Ann. *Chim. (Paris)* 1955, 10, 397.

5 E.M. Levin, C.R. Robbins and H.F. McMurdie, *Phase diagram for ceramists*, (compiled at the Nation Bureau of Standard, edited and published by the American Ceramic Society Inc., 1964, Fig. 51)

6 S. Yagi, Y. Ichikawa, I. Yamada, T. Doi, T. Ichitsubo and E. Matsubara, *Jap. J. Appl. Phys*., 2013, 52, 02501.

7 M.Y. Li and P. Shen, *Mater. Sci. Eng. B*, 2004, 111, 82.

8 W.H. Lee and P. Shen, *J. Solid State Chem*., 2004, 177, 101.

9 T.M. Tsai, K.C. Yang and P. Shen, *J. Solid State Chem.*, 2004, 177, 3301.

10 C.N.Huang, P. Shen and K.Y. Hsieh, *J. Eur. Ceram. Soc*., 2007, 27, 4685.

11 K.C.Yang and P. Shen, *J. Solid State Chem*., 2005, 178, 661.

12 K. An, N. Lee, J. Park, S.C. Kim, Y. Hwang, M.J. Han, J. Yu and T. Hyeon, *J. Am. Chem. Soc*., 2006, 128, 9753.

13 M.E. Baydi, G. Poillerat, J.L. Rehspringer, J.L. Gautier, J.F. Koenig and P. Chartier, *J. Solid State Chem*., 1994, 109, 281.

14 J. Ahmed, T. Ahmad, K.V. Ramanujachary, S.E. Lofland and A.K. Ganguli, *J. Colloid and Interface Sci*., 2008, 321, 434.

15 T. He, D.R. Chen, X.L. Jiao, Y.Y. Xu and Y.X. Gu, *Langmuir*, 2004, 20, 8404.

16 X.H. Liu, G.Z. Qiu and X.G. Li, *Nanotechnology*, 2005, 16, 3035.

17 X. Xie and W. Shen, *Nanoscale*, 2009, 1, 50.

18 D. Liu, X. Wang, W. Tian, Y. Bando and D. Golberg, *Scientific Reports*, 2013, 3, 2543.

19 X. Xiao, X. Liu, H. Zhao, D. Chen, F. Liu, J. Xiang, Z. Hu and Y. Li, *Adv. Mater*., 2012, 24, 5762.

20 Y. Wang, H.J. Zhang, J. Wei, C.C. Wong, J.Y. Lin and A. Borgna, *Energ. Environ. Sci*., 2011, 4, 1845.

21 E.V. Ilyina, I.V. Mishakov, A.A. Vedyagin and A.F. Bedilo, *J. Sol-Gel Sci. Tech*., 2013, 68, 423.

22. D. Liu, C. Li, F. Zhou, T. Zhang, H. Zhang, X. Li, G. Duan, W. Cai and Y. Li, *Scientific Reports,* 2015, **5**, 7686.

23. H. Zhang, Y. Li, G. Duan, G. Liu and W. Cai, *CrystEngComm*, 2014, **16**, 2491.

24. W. Wang, W. Yang, Z. Liu, Y. Lin, S. Zhou, H. Qian, F. Gao and G. Li, *CrystEngComm*, 2014, **16**, 4100.

25. W. Wang, W. Yang, Z. Liu, Y. Lin, S. Zhou, H. Qian, H. Wang, Z. Lin, S. Zhang, G. Li, *CrystEngComm*, 2014, **16**, 8500.

26 C.N. Huang, S.Y. Chen, M.H. Tsai and P. Shen, *J. Cryst. Growth*, 2007, 305, 285.

27 J.P. Poirier and A. Tarantola, *Phys. Earth Planet. Inter*., 1998, 109, 1.

28 J.P. Poirier, *Introduction to the physics of the Earth's interior*, Edition 2, (Cambridge University Press, Cambridge, 2000)

29 Y.W. Fei, *Am. Mineral*., 1999, **84**, 272.

30 S. Rekhi, S.K. Saxena, Z.D. Atlasa and J. Hub, *Solid State Commun*., 2001, 117, 33.

31 Q. Guo, H.K. Mao, J.Z. Hu, J.F. Shu and R.J. Hemley, *J. Phys.: Condens. Matter*, 2002, 14, 11369.

32 R.D. Shannon, *Acta Crystallogr A*, 1976, **32**, 751.

33 F.A. Kröger and H.J. Vink, *Solid State Phys*., 1956, 3, 307.

34 N.H. de Leeuw, G.W. Watson and S.C. Parker, *J. Phys. Chem*., 1995, 99, 17219.

35 M.L. Jeng and P. Shen, *Mater. Sci. Eng. A*, 2000, 287, 1.

36 J.J. Papike, *Planetary materials, in Reviews in Mineralogy* vol. 36, (series Editor: Ribbe P.H. Mineral. Soc. Am. 1998)

37 E.M. Logothesis, K. Park, A.H. Meitzler and K.R. Laud, *Appl. Phys. Lett*., 1975, 26, 209.

38 G.B. Smith, A. Ignatiev and G. Zajac, *J. Appl. Phys*., 1980, 51, 4186.

39 T. Maruyama and S. Arai, *J. Electrochem. Soc*., 1996, 143, 1383.

40 M. Ando, T. Kobayashi, S. Iijima and M. Haruta, *J. Mater. Chem*., 1997, **7**, 1779.

41 T.Y. Lin, S.S. Lin, S.Y. Chen and P. Shen, *CrystEngComm*, 2015, 17, 3468.

42 Y. Soneda, K. Szostak, S. Delpeux, S. Bonnamy, F. Béguin, AIP Conf. Proc. **591**, 199 (2001)

43 S. Delpeux, K. Szostak, E. Frackowiak, S. Bonnamy and F. Béguin, *J. Nanosci. Nanotech*., 2002, 2, 481.

44 V.V. Chesnokov, V.I. Zaikovskii and I.E. Soshnikov, *J. Phys. Chem. C*, 2007, 111, 7868.

Appendix 1. MgO-$Co_{1-x}O$ phase diagram for $P(O_2)$ = 0.21 atm (FACT oxide data base).

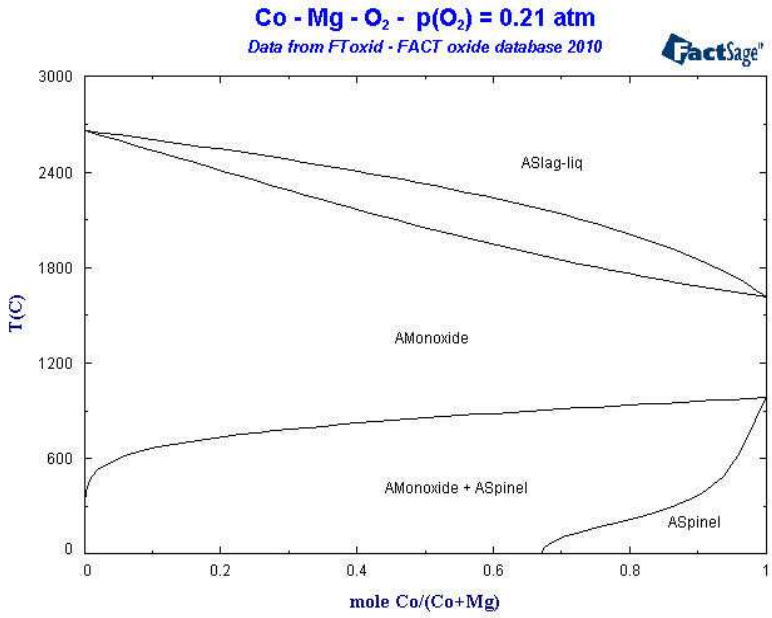

Appendix 2. Photos of solid solution targets (a) C1M9, (b) C5M5 and (c) C9M1 with pink, dark and gray color, respectively, in contrast with the laser ablated darkish trough (arrow).

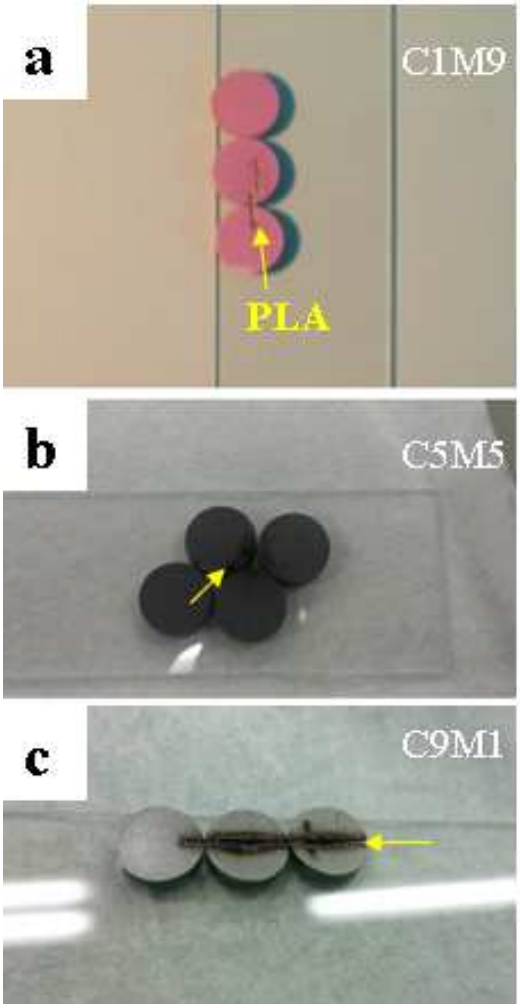

Figure captions

Figure 1. XRD (CuKα) trace of rocksalt type $(Co_xMg_{1-x})O$ condensates produced by PLA of (a) C1M9, (b) C5M5 and (c) C9M1 target for 5 min in air. Note weak peaks of minor Mg-doped $Co_{3-\delta}O_4$ spinel in (c).

Figure 2. TEM (a) BFI, (b) DFI (g=002) and (c) SAED pattern of rocksalt type $(Co_xMg_{1-x})O$ condensates with cubic shape and hence [100] preferred orientation as formed by PLA of C1M9 in air for 5 sec.

Figure 3. TEM (a) BFI, (b) DFI (g=$0\bar{2}\,\bar{2}$), (c) SAED pattern and (d) EDX spectrum of a rocksalt type $(Co_xMg_{1-x})O$ particulate with Co:Mg=1:19 which remained cubic-like shape having {110} ledges still decorated with {100} facets as formed by PLA of C1M9 in air for 5 sec. Note several cubic nanocondensates in parallel epitaxy with the particulate despite the surrounding of turbostratic graphene which was formed by the catalytic effect of the nanoparticles on the matrix of carbon-coated collodion film (cf. text).

Figure 4. TEM (a) lattice image, (b) and (c) 2-D forward/inverse Fourier transform of the square region in (a), showing parallel epitaxy coalescence of rocksalt type $(Co_xMg_{1-x})O$ cubic nanocondensates in the [100] zone axis with turbostratic graphene shell (denoted as G in a) and paracrystalline distribution of defect clusters (dot-like dark/bright contrast in c) as formed by PLA of C1M9 in air for 5 sec.

Figure 5. TEM (a) BFI, (b) DFI (g=$00\bar{2}$), (c) SAED pattern and (d) EDX spectrum of a rocksalt type $(Co_xMg_{1-x})O$ particulate (Co:Mg~1.4:1.0) with smaller-sized nanocondensates coalesced over (100) (top view in the [100] zone axis) to form (100) 26.6^o twist boundary as shown representatively by (e) lattice image and (f) 2-D Fourier transform of the square region in (a) with such a nanoparticle slightly off the [100] zone axis (cf. text). Sample as formed by PLA of C5M5 in air for 5 sec.

Figure 6. TEM (a) BFI, (b) SAED pattern and (c) EDX spectrum of rocksalt-type $(Co_xMg_{1-x})O$ particulate and nanocondensates (Co:Mg~10:1) in coalescence to exhibit (100), (111)

and~$(3\bar{1}\bar{1})$ faces edge on in the $[01\bar{1}]$ zone axis despite turbostratic graphene surrounding as formed by PLA of C5M5 in air for 15 sec.

Figure 7. TEM (a) BFI, (b) DFI (g= 200), (c) SAED pattern and (d) EDX spectrum of a nearly spherical rocksalt-type $(Co_xMg_{1-x})O$ particulate (Co:Mg~0.9:1.0 on the average) with (100) and (011) facets which was in parallel coalescence with a {100} and {011} faceted nanocondensate over its (100) surface as shown edge on in the $[01\bar{1}]$ zone axis. Note side band diffractions due to paracrystalline distribution of defect clusters. Sample as formed by PLA of C5M5 in air for 15 sec.

Figure 8. TEM (a) BFI, (b) SAED pattern and (c) EDX spectrum of two rocksalt type $(Co_xMg_{1-x})O$ nanocondensates (Co:Mg~8.3:1.0 on the average) coalesced over (100) to have a 2:1 aspect ratio in the [100] zone axis surrounded by turbostratic graphene, as formed by PLA of C9M1 in air for 5 sec. Note orthogonal planar diffraction contrast due to paracrystalline distribution of defect clusters in (b).

Figure 9. TEM (a) BFI, (b) SAED pattern and (c) EDX spectrum of a cubic-like Mg-doped $Co_{3-\delta}O_4$ spinel nanocondensate (Co:Mg~11.3:1.0) with side-band paracrystal diffraction (P) in the [100] zone axis as formed by PLA of C9M1 in air for 5 sec.

Figure 10. TEM (a) BFI, (b) SAED pattern and (c) EDX spectrum of a spherical-like Mg-doped $Co_{3-\delta}O_4$ spinel particulate (Co:Mg~11:1) with {011} and {121} facets edge one and paracrystal diffraction (P) in the $[11\bar{1}]$ zone axis as formed by PLA of C9M1 in air for 5 sec.

Figure 11. UV-visible absorption spectra of the condensates produced by PLA of (a) C1M9, (b) C5M5 and (c) C9M1 target for 5 min in air, showing absorbance peak extrapolation to 350, 375 and 390 nm corresponding to an apparent minimum band gap of 3.5, 3.3 and 3.2 eV, respectively. Note bimodal absorbance in (a) may be due to composition inhomogeneity of the $(Co_xMg_{1-x})O$ particulates/condensates.

Figure 12. Optical polarized micrographs (a) open polarizer, (b) crossed polarizers, (c) with

additional λ plate of rocksalt type $(Co_xMg_{1-x})O$ condensates/particulates collected/assembled on a silica glass plate by PLA of C1M9, C5M5 and C9M1 (from left to right) in air for 5 min, showing the brownish particulates and much smaller-sized particles are both slightly birefringent (cf. text).

Figure 13. CSL of (001) 26.6^o twist boundary of A/B bicrystal in the [001] zone axis having a rhombohedral CSL with 4.5x lattice parameter of the parental rocksalt-type structure and alternating mixed/unmixed charge along $2[210]_A//4.5[100]_B$ and $4.5[010]_A//2[120]_B$ directions.

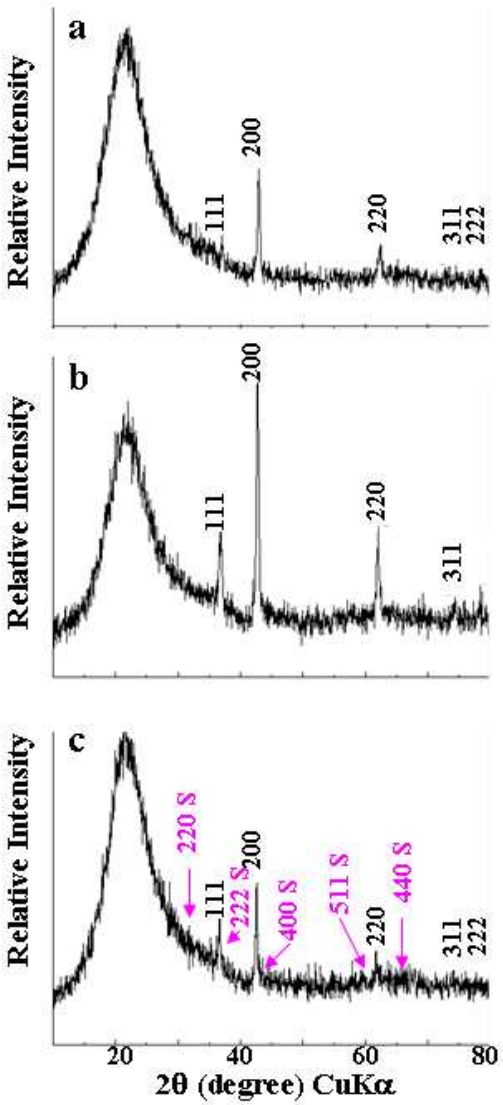

Figure 1. XRD (CuKα) trace of rocksalt type $(Co_xMg_{1-x})O$ condensates produced by PLA of (a) C1M9, (b) C5M5 and (c) C9M1 target for 5 min in air. Note weak peaks of minor Mg-doped $Co_{3-\delta}O_4$ spinel in (c).

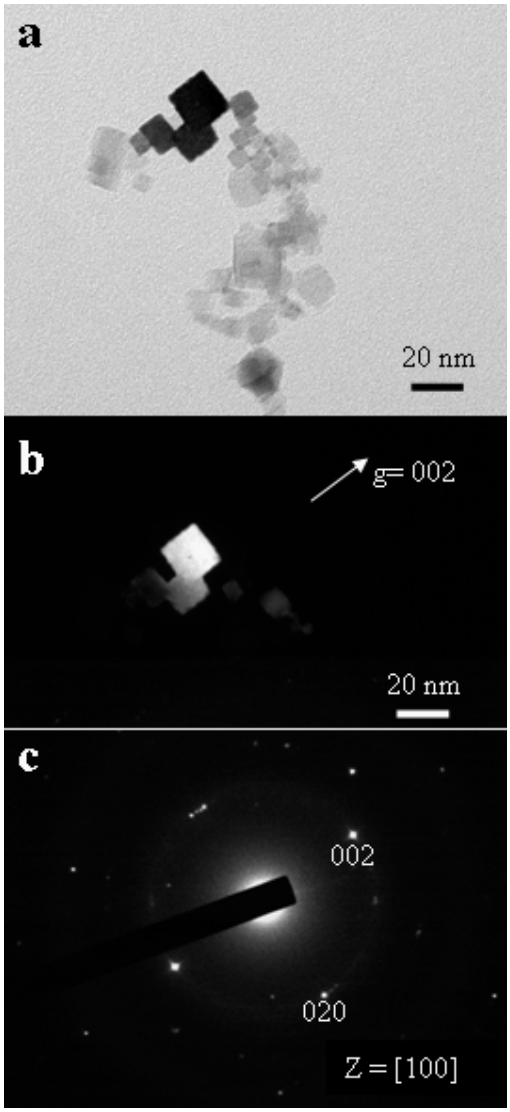

Figure 2. TEM (a) BFI, (b) DFI (g=002) and (c) SAED pattern of rocksalt type $(Co_xMg_{1-x})O$ nanocondensates/particulates with cubic shape and hence [100] preferred orientation as formed by PLA of C1M9 in air for 5 sec.

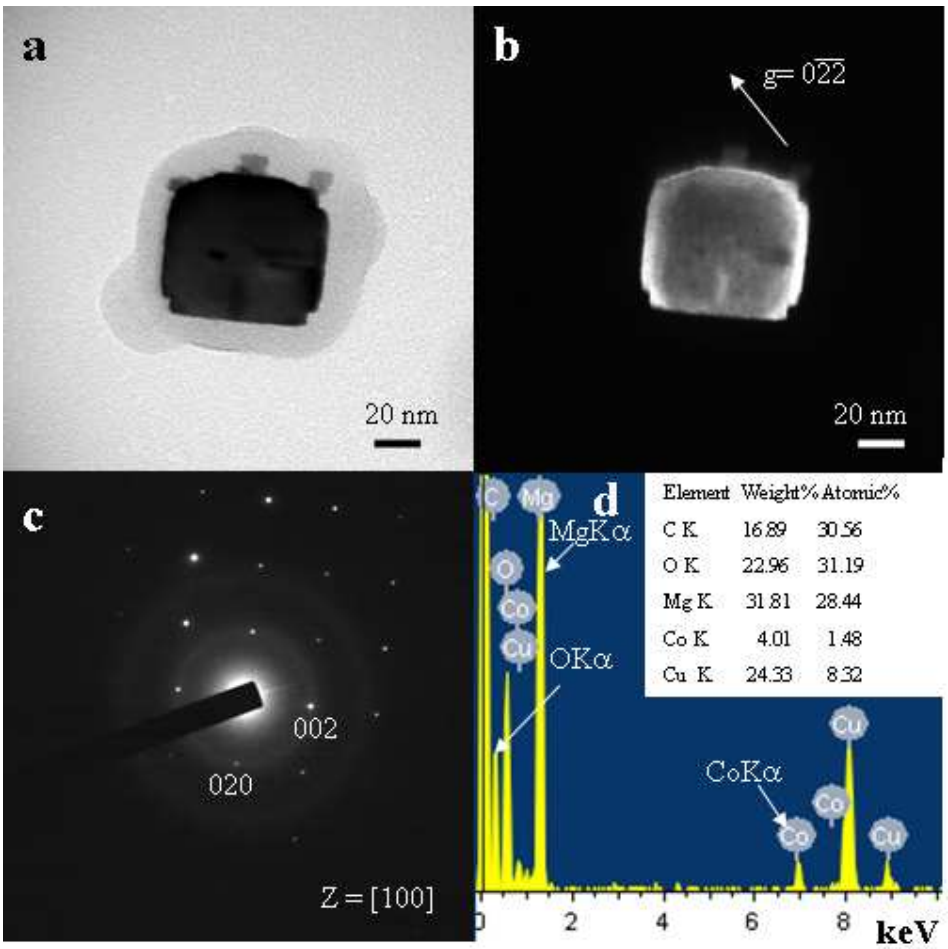

Figure 3. TEM (a) BFI, (b) DFI (g=0$\bar{2}\,\bar{2}$), (c) SAED pattern and (d) EDX spectrum of a rocksalt type (Co_xMg_{1-x})O particulate with Co:Mg=1:19 which remained cubic-like shape having {110} ledges still decorated with {100} facets as formed by PLA of C1M9 in air for 5 sec. Note several cubic nanocondensates in parallel epitaxy with the particulate despite the surrounding of turbostratic graphene which was formed by the catalytic effect of the nanoparticles on the matrix of carbon-coated collodion film (cf. text).

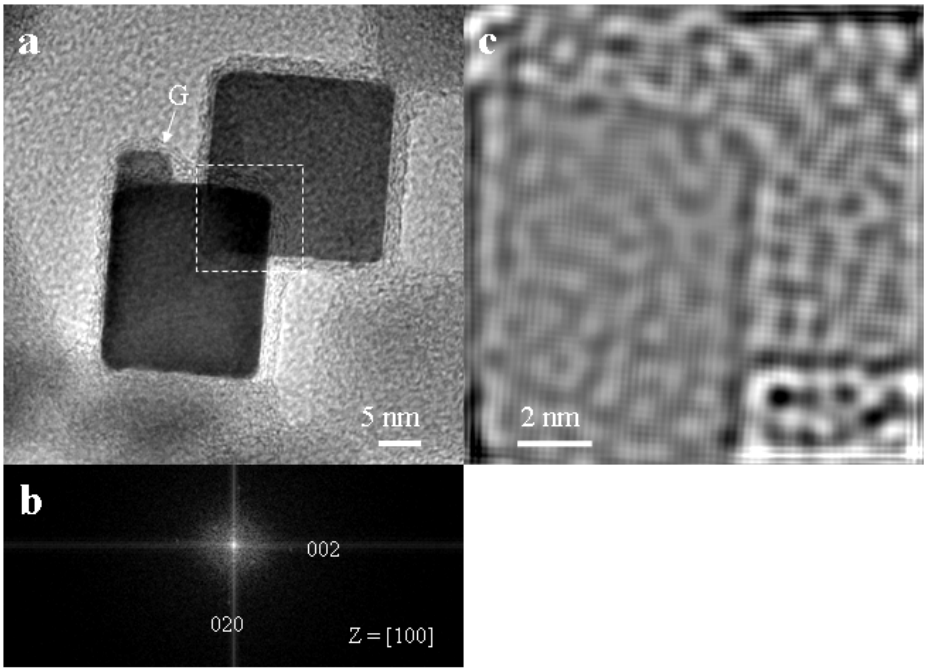

Figure 4. TEM (a) lattice image, (b) and (c) 2-D forward/inverse Fourier transform of the square region in (a), showing parallel epitaxy coalescence of rocksalt type $(Co_xMg_{1-x})O$ cubic nanocondensates in the [100] zone axis with turbostratic graphene shell (denoted as G in a) and paracrystalline distribution of defect clusters (dot-like dark/bright contrast in c) as formed by PLA of C1M9 in air for 5 sec.

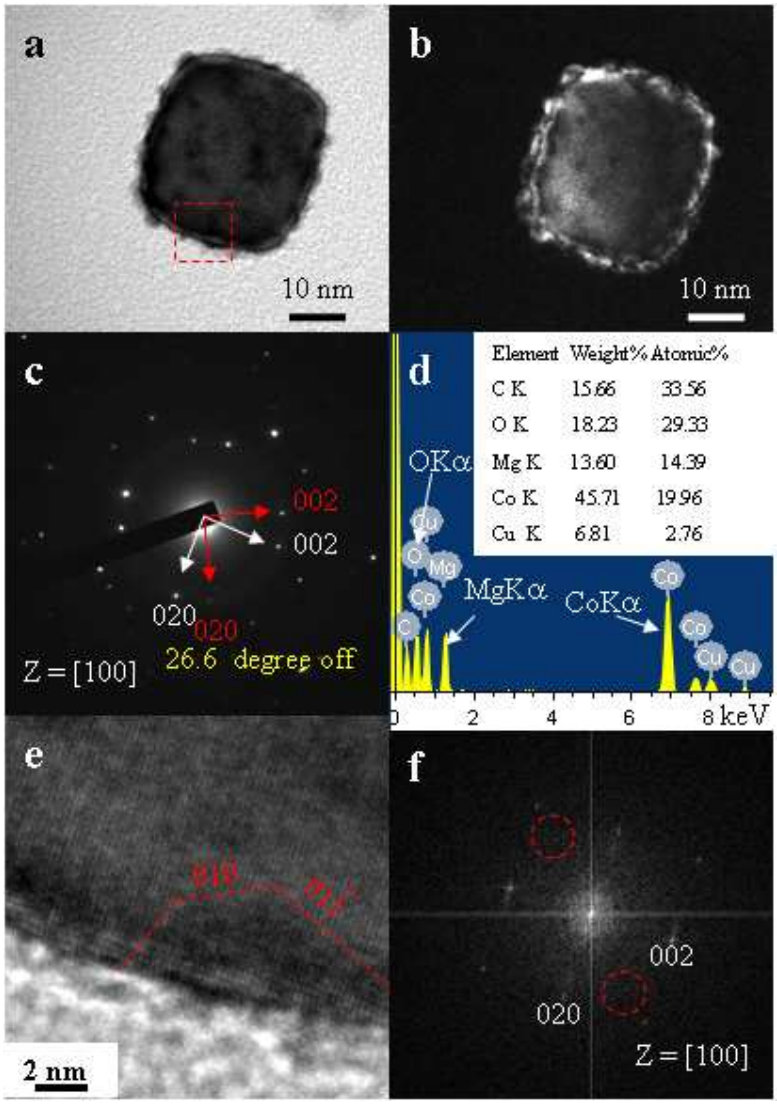

Figure 5. TEM (a) BFI, (b) DFI (g=00$\bar{2}$), (c) SAED pattern and (d) EDX spectrum of a rocksalt type (Co_xMg_{1-x})O particulate (Co:Mg~1.4:1.0) with smaller-sized nanocondensates coalesced over (100) (top view in the [100] zone axis) to form (100) 26.6^o twist boundary as shown representatively by (e) lattice image and (f) 2-D Fourier transform of the square region in (a) with such a nanoparticle slightly off the [100] zone axis (cf. text). Sample as formed by PLA of C5M5 in air for 5 sec.

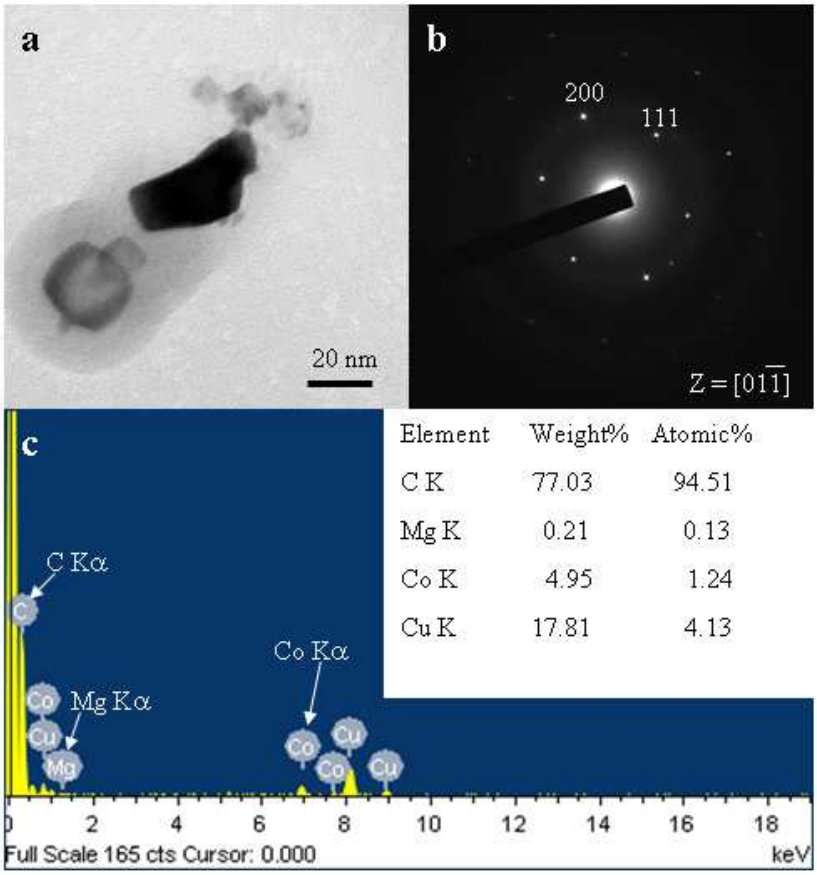

Figure 6. TEM (a) BFI, (b) SAED pattern and (c) EDX spectrum of rocksalt-type $(Co_xMg_{1-x})O$ particulates (Co:Mg~10:1) in coalescence to exhibit (100), (111) and~$(3\bar{1}\bar{1})$ faces edge on in the $[01\bar{1}]$ zone axis despite turbostratic graphene surrounding as formed by PLA of C5M5 in air for 15 sec.

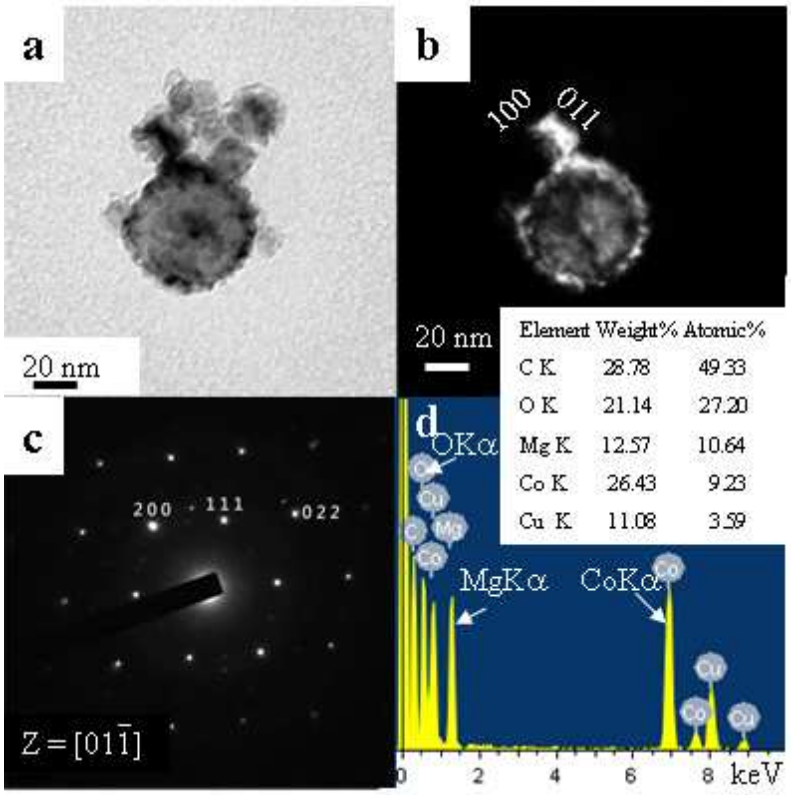

Figure 7. TEM (a) BFI, (b) DFI (g= 200), (c) SAED pattern and (d) EDX spectrum of a nearly spherical rocksalt-type $(Co_xMg_{1-x})O$ particulate (Co:Mg~0.9:1.0 on the average) with (100) and (011) facets which was in parallel coalescence with a {100} and {011} faceted nanocondensate over its (100) surface as shown edge on in the [01$\bar{1}$] zone axis. Note side band diffractions due to paracrystalline distribution of defect clusters. Sample as formed by PLA of C5M5 in air for 15 sec.

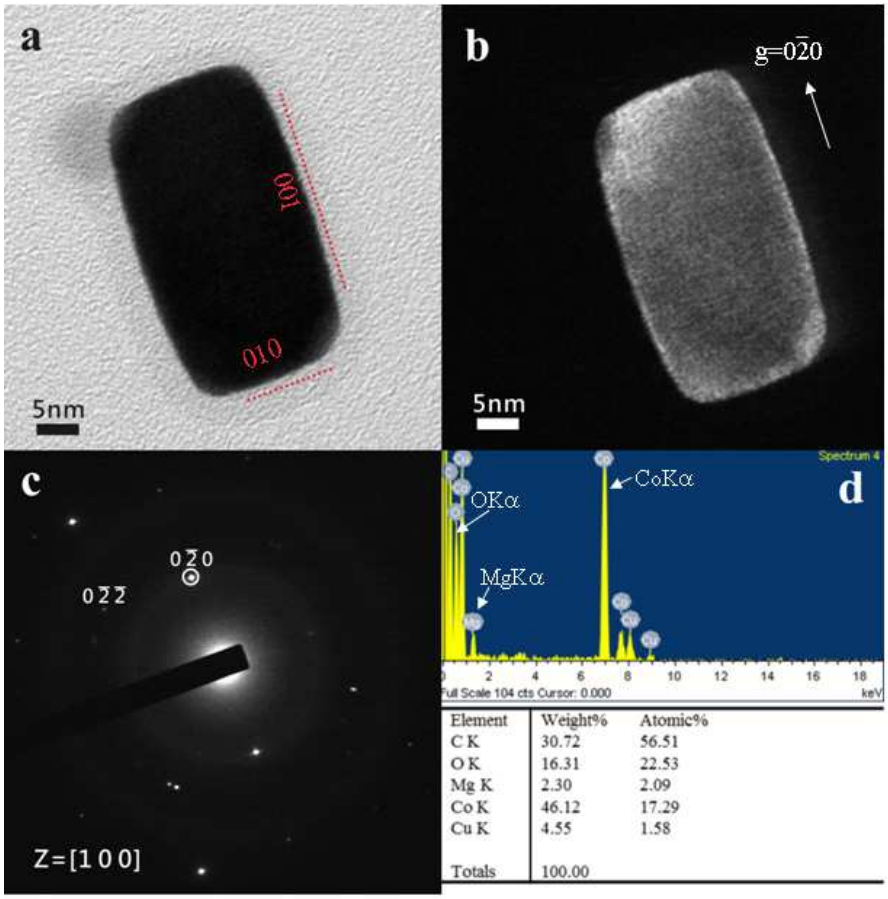

Figure 8. TEM (a) BFI, (b) SAED pattern and (c) EDX spectrum of two rocksalt type (Co_xMg_{1-x})O nanocondensates (Co:Mg~8.3:1.0 on the average) coalesced over (100) to have a 2:1 aspect ratio in the [100] zone axis surrounded by turbostratic graphene, as formed by PLA of C9M1 in air for 5 sec. Note orthogonal planar diffraction contrast due to paracrystalline distribution of defect clusters in (b).

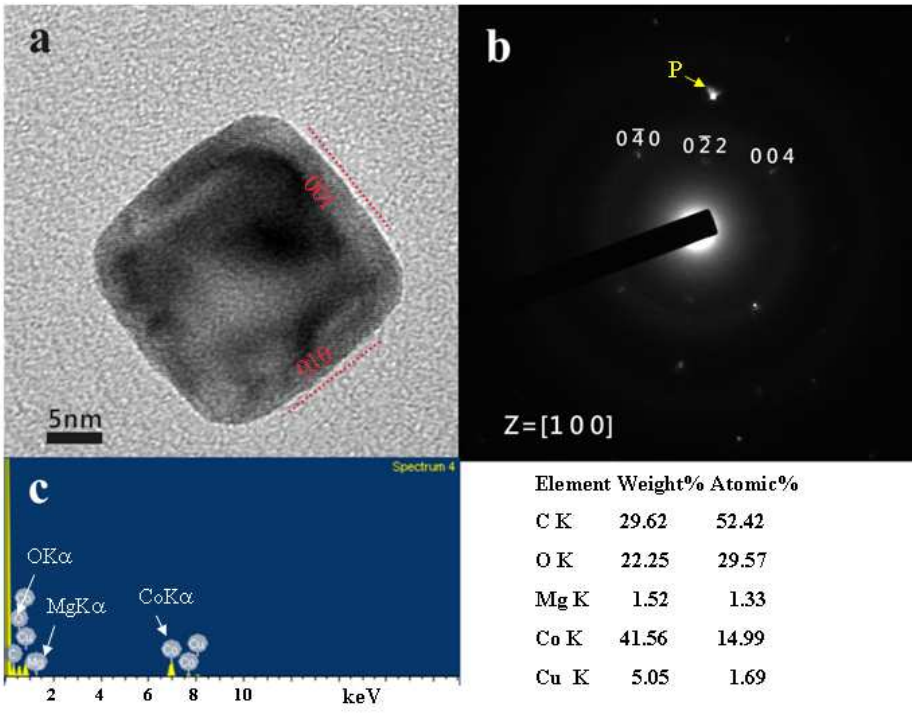

Figure 9. TEM (a) BFI, (b) SAED pattern and (c) EDX spectrum of a cubic-like Mg-doped $Co_{3-\delta}O_4$ spinel nanocondensate (Co:Mg~11.3:1.0) with side-band paracrystal diffraction (P) in the [100] zone axis as formed by PLA of C9M1 in air for 5 sec.

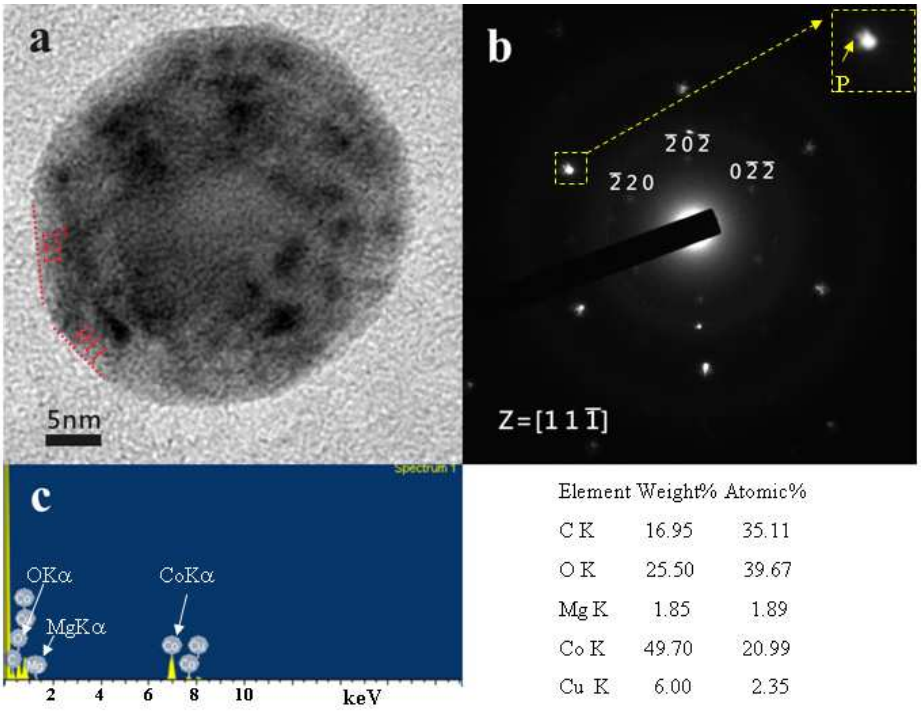

Element	Weight%	Atomic%
C K	16.95	35.11
O K	25.50	39.67
Mg K	1.85	1.89
Co K	49.70	20.99
Cu K	6.00	2.35

Figure 10. TEM (a) BFI, (b) SAED pattern and (c) EDX spectrum of a spherical-like Mg-doped $Co_{3-\delta}O_4$ spinel particulate (Co:Mg~11:1) with {011} and {121} facets edge one and paracrystal diffraction (P) in the [11$\bar{1}$] zone axis as formed by PLA of C9M1 in air for 5 sec.

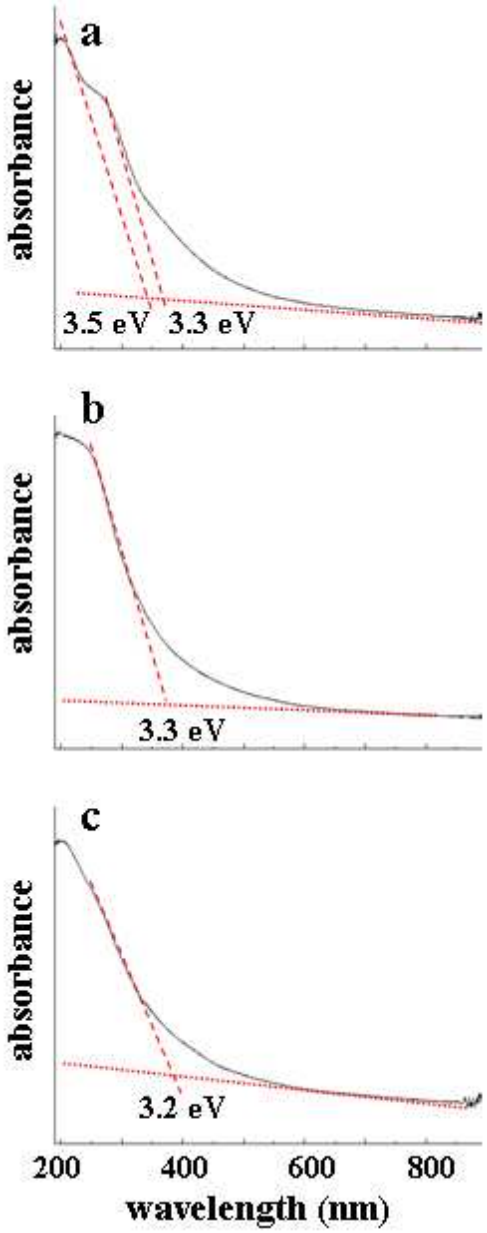

Figure 11. UV-visible absorption spectra of the condensates produced by PLA of (a) C1M9, (b) C5M5 and (c) C9M1 target for 5 min in air, showing absorbance peak extrapolation to 350, 375 and 390 nm corresponding to an apparent minimum band gap of 3.5, 3.3 and 3.2 eV, respectively. Note bimodal absorbance in (a) may be due to composition inhomogeneity of the $(Co_xMg_{1-x})O$ particulates/condensates.

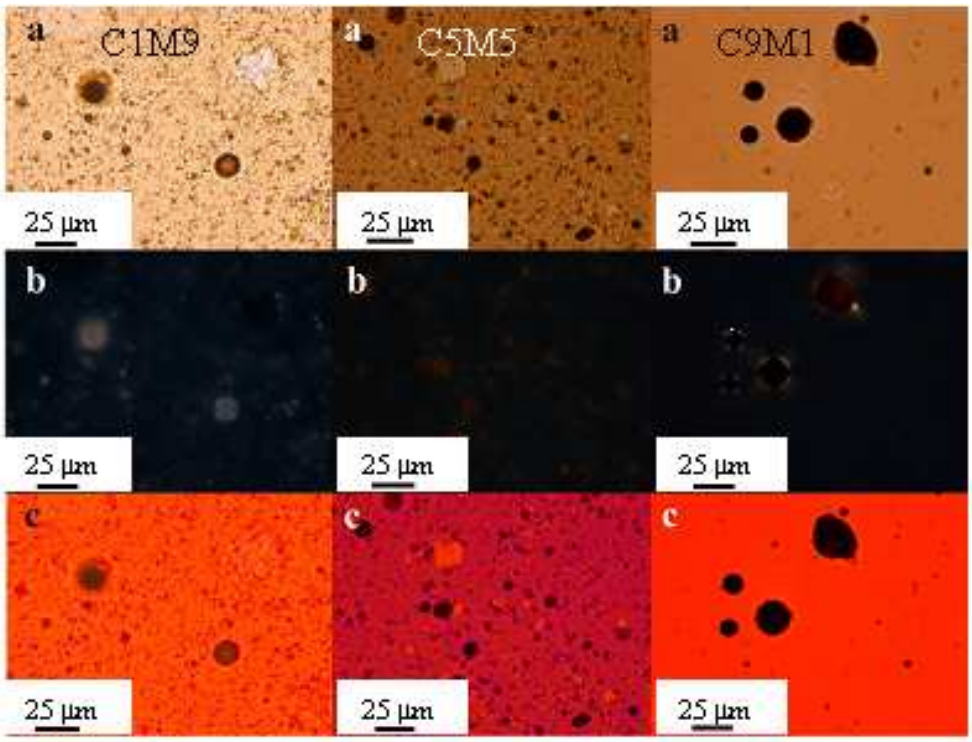

Figure 12. Optical polarized micrographs (a) open polarizer, (b) crossed polarizers, (c) with additional λ plate of rocksalt type $(Co_xMg_{1-x})O$ condensates/particulates collected/assembled on a silica glass plate by PLA of C1M9, C5M5 and C9M1 (from left to right) in air for 5 min, showing the brownish particulates and much smaller-sized particles are both slightly birefringent (cf. text).

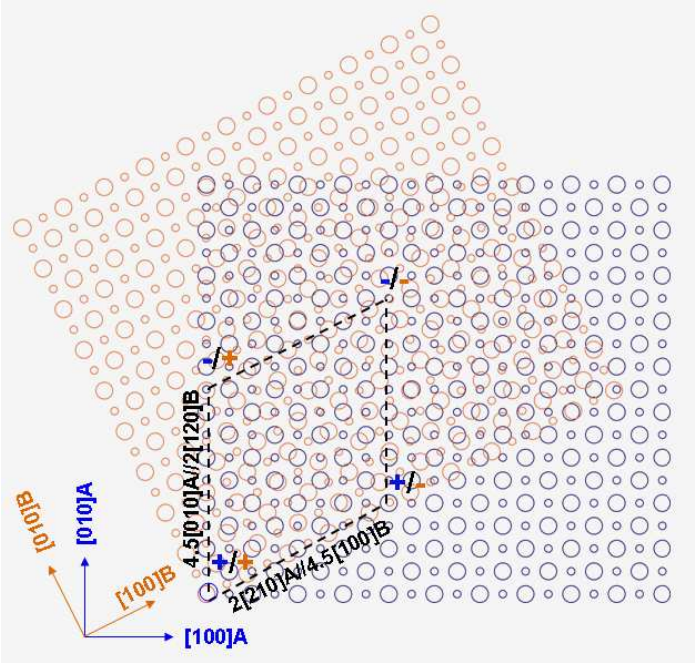

Figure 13. CSL of (001) 26.6° twist boundary of A/B bicrystal in the [001] zone axis having a rhombohedral CSL with 4.5x lattice parameter of the parental rocksalt-type structure and alternating mixed/unmixed charge along $2[210]_A//4.5[100]_B$ and $4.5[010]_A//2[120]_B$ directions.

TOC

(Co,Mg)O nanocondensates produced by pulsed laser ablation of MgO-CoO solid solution target in air